Disorder-dependent superconducting phase diagram at high magnetic fields in $Fe_{1+y}Se_xTe_{1-x}$ ($x \sim 0.4$)

T. Gebre,[1] G. Li,[1] J. B. Whalen,[1,2] B. S. Conner,[1] H. D. Zhou,[1] G. Grissonnanche,[1] M. K. Kostov,[1,2] A. Gurevich,[1,3] T. Siegrist,[1,2] and L. Balicas[1,*]

[1]*National High Magnetic Field Laboratory, Florida State University, Tallahassee, Florida 32310, USA*

[2]*Department of Chemical and Biomedical Engineering, FAMU-FSU College of Engineering, Tallahassee, Florida 32310, USA*

[3]*Physics Department, Old Dominion University, Norfolk, Virginia 23529, USA*

(Received 10 June 2011; revised manuscript received 18 August 2011; published 21 November 2011)

We compare the superconducting phase-diagram under high magnetic fields (up to $H = 45$ T) of $Fe_{1+y}Se_{0.4}Te_{0.6}$ single crystals originally grown by the Bridgman-Stockbarger (BRST) technique, which were annealed to display narrow superconducting transitions and the optimal transition temperature $T_c \gtrsim 14$ K, with the diagram for samples of similar stoichiometry grown by the traveling-solvent floating-zone technique as well as with the phase diagram reported for crystals grown by a self-flux method. We find that the so-annealed samples tend to display higher ratios H_{c2}/T_c, particularly for fields applied along the interplanar direction, where the upper critical field $H_{c2}(T)$ exhibits a pronounced concave down curvature followed by saturation at lower temperatures T. This last observation is consistent with previous studies indicating that this system is Pauli limited. An analysis of our $H_{c2}(T)$ data using a multiband theory suggests the emergence of the Fulde-Ferrel-Larkin-Ovchnikov state at low temperatures. A detailed structural x-ray analysis, reveals no impurity phases but an appreciable degree of mosaicity in as-grown BRST single crystals that remains unaffected by the annealing process. Energy-dispersive x-ray analysis showed that the annealed samples have a more homogeneous stoichiometric distribution of both Fe and Se with virtually the same content of interstitial Fe as the nonannealed ones. Thus we conclude that the excess of Fe, in contrast to structural disorder, contributes to the decrease of the superconducting upper-critical fields of this series. Finally, a scaling analysis of the fluctuation conductivity in the superconducting critical regime, suggests that the superconducting fluctuations have a two-dimensional character in this system.

DOI: 10.1103/PhysRevB.84.174517 PACS number(s): 74.70.Xa, 74.25.Dw, 74.62.Dh, 74.25.fc

I. INTRODUCTION

The Fe_{1+y}(Te,Se) series is a quite unique superconducting system; its end member, FeSe, is a superconductor with a superconducting transition temperature $T_c \simeq 8$ K,[1] which can be increased up to ~14 K with the partial substitution of Se for Te[2,3] or increased all the way up to 36.7 K by the application of hydrostatic pressure.[4] The other end member of this series, $Fe_{1+y}Te$, is not superconducting and instead exhibits a simultaneous structural and magnetic phase transition from tetragonal to monoclinic symmetry accompanied by antiferromagnetism (AFM) near $T_N \simeq 60$ to 70 K (Refs. 5–7). This AFM structure is distinct from those seen in the undoped FeAs-based compounds.[8–10] The AFM order in $Fe_{1+y}Te$ propagates along the diagonal direction of the original undistorted Fe square lattice,[5,7] while in FeAs the wave vector of the spin-density wave (SDW) propagates along the nearest-neighbor direction of the original Fe square lattice.[8–10]

Density functional theory (DFT) calculations indicate that the Fermi surfaces (FS) of both FeSe and FeTe are similar to those of the other FeAs-based compounds, consequently, they should satisfy the nesting condition for the wave vector $Q_{\pi,\pi} = (\pi,\pi)$.[11] This apparent lack of universality would seem to question the exclusive role of the interband pairing via $Q_{\pi,\pi}$ magnetic fluctuations in the pairing mechanism for all the iron-based superconductors. However, the observation of a spin resonance below T_c together with an enhancement of the spin fluctuations near it, indeed suggests a spin fluctuations mediated superconducting pairing mechanism for this system.[12,13] Initial angle-resolved photoemission spectroscopy (ARPES) measurements in the $Fe_{1+y}Te$ revealed a pair of nearly compensated electron-hole FS pockets, with no evidence for the FS nesting instability associated with $Q_{\pi,\pi}$.[14] This could suggest the possibility of a distinct mechanism for the superconductivity and the magnetic order in the Fe chalcogenides when compared to the Fe arsenides. But a recent ARPES study on superconducting $Fe_{1.03}Te_{0.7}Se_{0.3}$ reveals a holelike and an electron-like FS located at the center and at the corner of the Brillouin zone, respectively. These FSs are nearly nested for $Q_{\pi,\pi}$.[15] The same study reports an isotropic superconducting gap along the hole-like FS with a gap Δ of ~4 meV ($2\Delta = k_B T_c \sim 7$), thus providing evidence for strong-coupling superconductivity. But this is in contrast with a recent angle-dependent heat capacity study in $Fe_{1+y}Se_{0.45}Te_{0.55}$, which finds evidence for a significant gap anisotropy on the electron pockets.[16] Superconductivity in $Fe_{1+y}Se$ was shown to be extremely sensitive to stoichiometry.[17] In the Fe_{1+y}(Te,Se) series, the crystal structure resembles that of the iron arsenides[1] with the Fe square planar sheets forming from the edge-sharing iron chalcogen tetrahedral network. But it also allows the partial occupation of iron in the interstitial sites of the (Te, Se) layers, resulting in a nonstoichiometric composition for the Fe_{1+y}(Te,Se) series, where y represents the excess Fe at the interstitial sites.[5,6] It remains unclear how the geometry of the FS evolves with the incorporation of interstitial Fe, but it is claimed to suppress superconductivity.[18]

One remarkable feature of these compounds is their extremely large upper critical fields H_{c2}. For instance, according

to Ref. 19, for a $Fe_{1.05}Te_{0.89}Se_{0.11}$ single crystal with a middle point T_c of just 11 K, one observes an $H_{c2}(T \to 0\ \mathrm{K})$ of ~35 T, or for a single crystal of $Fe_{1.11}Te_{0.6}Se_{0.4}$ with a T_c close to its optimum value of 14 K one obtains $H_{c2}(T \to 0\ \mathrm{K})$ of ~40–45 T.[20] Compare these values with those of, for instance, MgB_2 single crystals, $T_c = 39$ K with $H^c_{c2}(0) = 3.5$ T and $H^{ab}_{c2}(0) = 17$ T, for fields along the c axis and along a planar direction, respectively.[21] In fact, to achieve in MgB_2 upper critical fields as large as those observed in the Fe_{1+y}(Te,Se) series, strong impurity scattering is introduced to optimize the relative strengths of intraband scattering in the σ and π bands of MgB_2.[22,23] The significant differences between these two multiband superconducting families are attributed to the fact that the Fe_{1+y}(Te,Se) superconductors are mostly Pauli limited,[19] while the H_{c2}s in MgB_2 are mostly determined by the orbital pair-breaking effect. However, the shape of the $H_{c2}(T)$ curves for the Fe_{1+y}(Te,Se) series measured in Refs. 19 and 20 are quite distinct, with the former presenting a nearly linear dependence for $H_{c2}(T)$ when $\mathbf{H} \| c$ and the second displaying a pronounced concave down curvature followed by saturation at lower temperatures (as expected for the Pauli-limiting effect). Such a curvature has also been reported in Ref. 24.

The Pauli-limited behavior of $H_{c2}(T)$ for the Fe-chalcogenides results from the fact that they are semimetals with rather low carrier density and low Fermi energies ~20–50 meV for different FS pockets,[14,15] unlike the conventional metallic superconductor MgB_2. As a result, chalcogenides have very short coherence lengths $\xi_0 \simeq \hbar v_F/2\pi T_c < 1$ nm and thus extremely high orbitally limited $H^{\mathrm{orb}}_{c2} \sim \phi_0/2\pi\xi^2$, where v_F is the Fermi velocity in the ab plane and ϕ_0 is the flux quantum. This, in turn, greatly enhances the Pauli effects quantified by the Maki parameter $\alpha_M = \sqrt{2}H^{\mathrm{orb}}_{c2}/H_p$, where $H_p\,(\mathrm{in\ T}) = 1.84T_c\,(\mathrm{in\ K})$ is the Clogston paramagnetic limit.[25] Chalcogenides typically have $\alpha_M \gtrsim 1$ above the critical value at which the Fulde-Ferrel-Larkin-Ovchinnikov (FFLO) instability develops. Moreover, because of their very short values of ξ_0, chalcogenides are naturally in the clean limit $\ell \gg \xi_0$, which is one of the conditions of the FFLO instability, where ℓ is the mean-free path due to elastic impurity scattering.[25] These features of chalcogenides make them good candidates to study exotic effects at high magnetic fields, in particular, the interplay of orbital and paramagnetic pair breaking for multiband pairing and the FFLO state at low temperatures. The small Fermi energies also make superconducting properties very sensitive to the doping level, allowing one to tune H_{c2} by small shifts of the chemical potential.

In contrast to other reports emphasizing on the details concerning the synthesis of single crystals,[26] in this work, we compare the high-field phase diagram of the Fe_{1+y}(Te,Se) series, particularly the diagram for the optimally doped compound $Fe_{1+y}Te_{(1-x)\approx 0.6}Se_{x\approx 0.4}$ synthesized by two methods. The first one is based on a traveling-solvent floating zone growth technique (TSFZ), which leads to crystals of acceptable crystallinity displaying "nonmetallic" resistivity, optimal T_cs, and transition widths $\Delta T_c \simeq 1$ to 3 K. We compare their behavior with crystals resulting from the Bridgman-Stockbarger (BRST) technique, which, in our case, leads to crystals displaying wider transitions and frequently to nonoptimal T_cs in as grown crystals, as previously reported by other groups.[27] These last single crystals were subjected to an annealing procedure that leads to metallic resistivity, considerably sharper resistive transitions $\Delta T_c \simeq 1$ K, and to superconducting transitions comparable to those reported in the literature for high-quality BRST-grown single crystals as measured by SQUID magnetometry.[28] The annealed crystals having a clear metallic behavior preceding superconductivity, display considerably higher upper critical fields when compared to those showing a poor metallicity, particularly for magnetic fields applied along the interlayer direction. This increase leads to a distinct shape of the $H^c_{c2}(T)$, i.e., from an approximately linear in T behavior as reported in Ref. 20, to the marked concave-down curvature followed by saturation at lower temperatures as seen in Ref. 24. The analysis of our experimental data using a multiband theory of $H_{c2}(T)$[29] shows that $H_{c2}(T)$ is indeed strongly Pauli limited $\alpha_M \simeq 7$–10, predicting the FFLO state below ≈5 K. A detailed single-crystal x-ray analysis reveals that the annealing process does not affect the crystallinity or the degree of mosaicity of our single crystals. Nevertheless, our dispersive x-ray analysis indicates that the annealing process leads to a more uniform distribution of interstitial Fe. Annealing yields a considerably more isotropic phase diagram, which combined with the enhancement in $H^c_{c2}(T)$, suggests that the variations in the content of interstitial Fe contributes to the suppression of superconductivity. Finally, we show, through a scaling analysis of the fluctuation conductivity in the neighborhood of the superconducting transition that the superconducting fluctuations in this system are two-dimensional in character.

II. SAMPLE PREPARATION

Single crystals of $Fe_{1+x}Te_{1-y}Se_y$, $0.05 \leqslant x \leqslant 0.15$ and $0.1 \leqslant y \leqslant 0.5$ were grown by using the traveling-solvent floating-zone growth (TSFZ) and the Bridgman-Stockbarger (BRST) techniques. Starting materials with nominal purities of 4N for Fe and 5N for Te and Se were used. These were handled in an argon-filled glove box, which kept the oxygen content below 1 ppm. Mixtures of Fe, Te, and Se were ground and pelletized and sealed in quartz ampoules under vacuum and heated at 400 °C for 24 h. The reacted material was reground and doubly sealed in two quartz ampoules. For samples grown through the TSFZ technique, the doubly sealed quartz ampoules were loaded into an optical floating-zone furnace (NEC Nichiden Machinery 15HD), equipped with two 1500 W halogen lamps. The ampoule was rotated at 20 rpm, and translated at a rate of 1 to 2 mm/h. The as-grown samples were annealed by heating to 800 °C for 48 h, and then cooled at a rate of 100 °C/h to 420 °C and held at this temperature for additional 30 h, followed by the cooling of the furnace to room temperature.

A double-wall quartz ampoule was also used in the case of crystals grown by the BRST technique. The inner ampoule was narrowly tipped at its bottom and sealed at the top. This Bridgman ampoule was inserted into a three-zone temperature gradient vertical furnace and lowered at a speed of 4 mm/h. The growth temperature was decreased at a rate of 3 °C/h down to 440 °C and subsequently quenched to room temperature.

Some of the crystals as well as Se powder were placed into two different quartz crucibles, and both placed inside an evacuated quartz ampoule that was sealed under vacuum, heated slowly to 400 °C, and then annealed for ten days.

The so-obtained crystals were checked by both single crystal and powder x-ray diffraction (XRD) techniques. From as-grown single crystals, shards were cleaved to obtain suitable samples of approximately 0.3 mm × 0.3 mm × 0.03 mm. An Oxford-Diffraction Xcalibur-2 CCD diffractometer with Mo K_α source was used to collect reflections. CRYSALIS PRO 171.33.55 software (Oxford Diffraction) was used for the unit-cell refinement and analytical absorption correction. Final structure refinements were conducted using SHELXTL. For the powder diffraction runs, the single crystals were ground by hand for approximately 1 minute using an agate mortar and pestle. Patterns were recorded by a Huber-Guinier G670 camera with a Rigaku Ultrax Cu K_α direct drive rotating anode source. WINPOW software was used for unit-cell parameter least-squares calculations and peak fitting. Further details are provided in Ref. 30.

Scanning electron-microscope energy-dispersive x-ray analysis (SEM-EDX) was performed by using a JEOL 5900 scanning electron microscope (30 kV accelerating voltage) equipped with IXRF energy dispersion spectroscopy software (IXRF Systems, Inc.) in order to determine the elemental compositions of the single crystals. We found that this EDX setup would show a tendency to underestimate by nearly 3% the overall fraction of Fe when comparing with detailed single-crystal x-ray refinements. We must clarify that the EDX setup was not calibrated against an absolute standard.

Longitudinal resistivity was measured using a conventional four-contact method in continuous magnetic fields up to 45 T by using either a physical property measurement system (PPMS) or the hybrid magnet of the National High Magnetic Field Laboratory in Tallahassee.

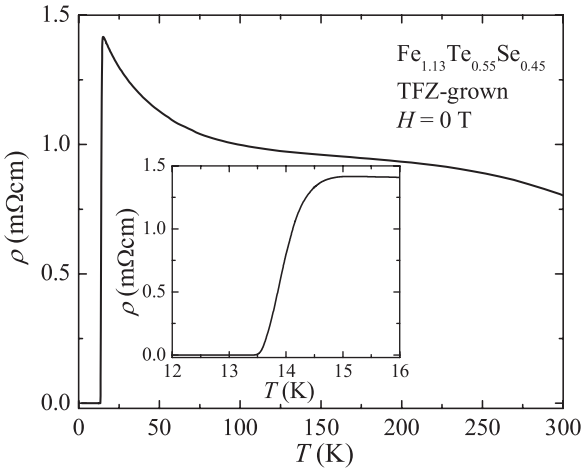

FIG. 1. (Color online) Resistivity as a function of temperature for a $Fe_{1.13}Se_{0.45}Te_{0.55}$ single crystal synthesized by the traveling floating zone method under zero magnetic field. Inset: resistive superconducting transition under zero field in a limited temperature range.

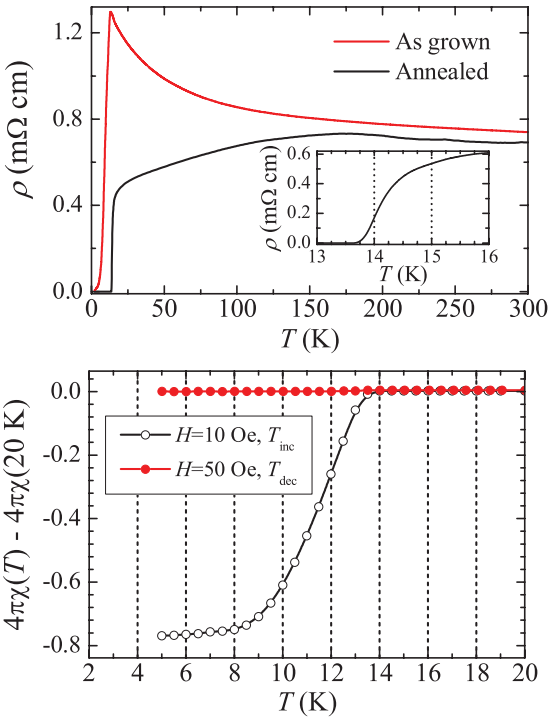

FIG. 2. (Color online) Top panel: resistivity as a function of temperature for an as-grown $Fe_{1.11}Se_{0.4}Te_{0.6}$ single crystal (nominal concentration), synthesized through the Bridgman-Stockbarger method (red curve) and under zero magnetic field. After annealing, the sample no longer displays the weak-localization-like temperature dependence. Instead, it displays a metallic character (black trace). Inset: superconducting resistive transition for the annealed crystal under zero field and in a limited temperature range. Bottom panel: magnetic susceptibility as a function of T for the same annealed single-crystal and respectively, for magnetic-field-cooled (red markers) and zero-field-cooled conditions (black markers).

III. SAMPLE CHARACTERIZATION

Figure 1 shows a typical trace of resistivity ρ as a function of the temperature for a single crystal grown by the traveling-solvent floating-zone method described above, whose stoichiometry was extracted by a detailed single-crystal x-ray analysis refinement. Although the width $\Delta T_c \sim 1$ K of the superconducting transition (see inset) is relatively narrow when compared with the width of the transitions shown for instance in Ref. 19, the behavior of the metallic state shows the typical negative slope $\partial\rho/\partial T < 0$ or logarithmic divergence of the resistivity. This was attributed to the high content of interstitial Fe which leads to weak localization.[18] The same characteristic temperature-dependent resistive behavior is observed also in as-grown samples synthesized by the Bridgman-Stockbarger method (red line), as seen in the top panel of Fig. 2. As seen, the as-grown samples tend to exhibit lower superconducting transition temperatures and broader transitions. The annealing procedure described above leads to a slightly smaller resistivity at room temperature (black line) but most importantly to a quite distinct temperature dependence for the resistivity, which below $T \sim 175$ K exhibits a clear metallic dependence with $\partial\rho/\partial T > 0$. The magnetic susceptibility on the other hand, shows a very clear diamagnetic signal

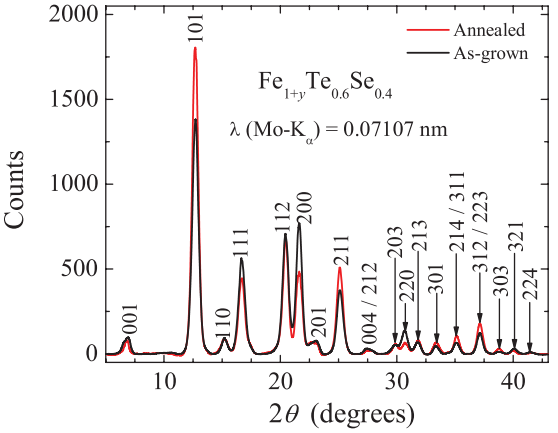

FIG. 3. (Color online) Powder x-ray diffraction pattern for two $Fe_{1.11}Se_{0.4}Te_{0.6}$ single crystals grown through the Bridgman technique, collected by using the Mo-K_α line. Black line corresponds to the spectrum of an as-grown crystal, while the red line is the spectrum obtained from a subsequently annealed single crystal. In both cases, well defined Bragg peaks are observed and indexed within the space group $P4/nmm$. We find no evidence for impurity phases or a change in structure/stoichiometry induced by the annealing process.

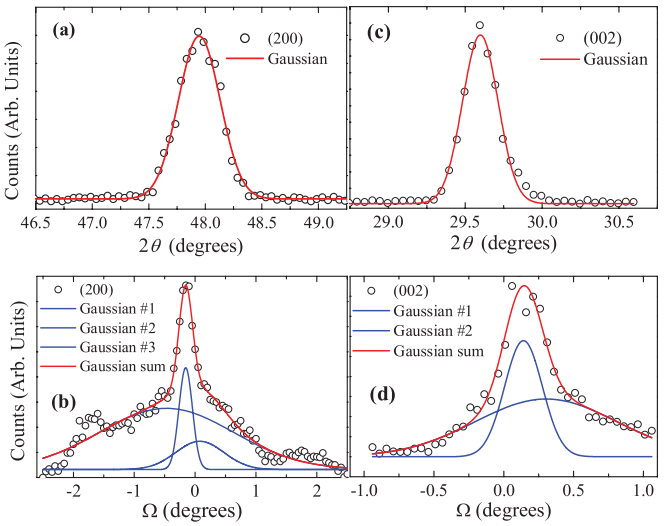

FIG. 4. (Color online) (a) X-ray intensity for an as-grown BS single crystal as a function of 2θ for an angular scan around the Bragg-peak observed along the real-space direction $(abc) = (200)$. Red line is a fit to a Gaussian function that yields a full width at half maximum of $\sim 0.5^\circ$. (b) X-ray rocking curve around the Bragg peak at (200) as a function of the angle Ω, which corresponds to an arc along a direction nearly perpendicular to θ. One observes a very broad feature that can be adjusted to three Gaussian distributions (blue lines) of crystallite orientations. (c) Same as in (a) but for a Bragg peak centered at the (002) position. Red line is a fit to a Gaussian having a full width at half maximum of $\sim 0.25^\circ$. (d) Same as in (b) but for the peak around the (002) position, although in this case, two Gaussian distributions are needed to adjust the observed broad peak.

(black markers) below the onset of T_c at $T = 14$ K, as seen in the lower panel of Fig. 2. At higher temperatures, the magnetic susceptibility is virtually temperature independent, as reported in Ref. 31, and only at low temperatures one observes a very mild upturn in the susceptibility suggesting the presence of a small amount of localized magnetic moments. Although none of the susceptibility traces in Ref. 31 shows a clear diamagnetic signal below $T_c \simeq 14$ K, but only below ~ 10 K.

We also characterized our single crystals through single-crystal and powder x-ray diffraction measurements. Figure 3 shows two typical powder x-ray spectra for one as-grown BRST crystal (black line) with a nominal stoichiometry $Fe_{1.11}Se_{0.4}Te_{0.6}$, and for one annealed BRST single crystal (red line) from the same batch. These "powder" patterns were produced from integrating the intensities from single-crystal x-ray diffraction measurements using an area detector. This powderlike pattern was obtained on the same single crystals used for the magnetic and transport measurements shown throughout this manuscript, by superimposing all of the θ to 2θ scans along the different crystallographic orientations. As clearly seen, for both crystals, we observe the same set of well defined Bragg peaks, where all peaks can be indexed within the tetragonal unit cell having the space group symmetry $P4/nmm$. Most importantly, we do not detect the presence of any impurity phase in either crystal, concluding that the annealing process preserves the original crystallographic structure and therefore the stoichiometry of the crystals. From this first analysis, it would seem that both crystals are equivalent in structural quality despite their marked differences in physical behavior as seen in the top panel of Fig. 2.

To clarify if disorder and mosaicity is at the origin of these differences in physical behavior, we performed a detailed x-ray rocking curve analysis in both single crystals around specific Bragg peaks. Figure 4(a) shows the (200) Bragg reflection. By fitting the intensity as a function of 2θ to a Gaussian distribution, one obtains a full width at half maximum (FWHM) of $\sim 0.5^\circ$, suggesting, at first glance, a modest but sizable mosaic spread among crystallites. However, an exploration of the width of this peak along an arc Ω whose orientation is nearly perpendicular to 2θ reveals a very broad feature as seen in Fig. 4(b). This broad maximum can be adjusted (red line) to three Gaussian distributions (blue lines), with one of them showing a FWHM as large as $\gtrsim 2.5^\circ$. Each Gaussian would represent an ensemble or distribution of crystallites having a similar relative orientation. The observation of several distributions with varying widths indicates a large degree of mosaicity around the (200) position or within the planes. A similar study around the (002) position shown respectively in Figs. 4(c) and 4(d), reveals seemingly a smaller degree of mosaicity among crystallites within distinct planes.

To clarify if the annealing process affects the structural degrees of freedom, for instance, by releasing strain induced in the single crystals by the synthesis process, we have attempted a similar detailed structural analysis in an annealed single crystal of $Fe_{1+y}Te_{0.6}Se_{0.4}$. Figure 5(a) shows the intensity of the Bragg peak located along the (200) direction as a function of the angle 2θ, while Fig. 5(b) shows the intensity of the same peak as a function of the angle Ω. The first measurement leads to a Gaussian peak (red line) having a FWHM of $\simeq 0.4^\circ$, while the second one can be adjusted to two Gaussian distributions (blue lines) with the widest distribution having a FWHM of $\simeq 1.6^\circ$. Figure 5(c) shows the intensity of the Bragg peak

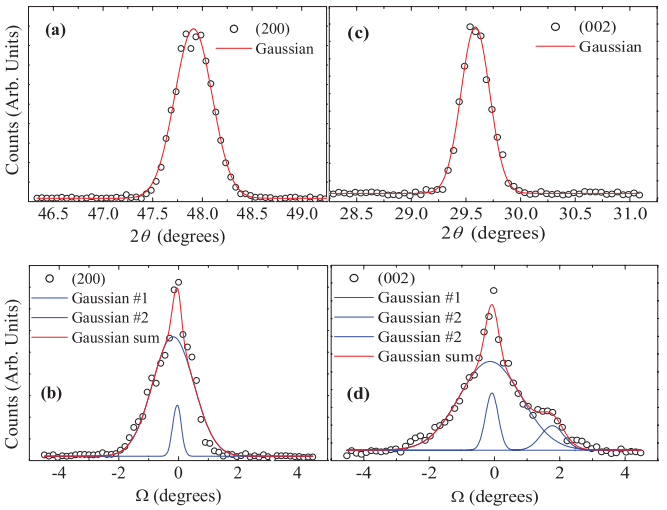

FIG. 5. (Color online) (a) X-ray intensity for an annealed BRST single-crystal of $Fe_{1+y}Te_{0.6}Se_{0.4}$ as a function of 2θ for an angular scan around the Bragg-peak observed along the real-space position $[abc] = (200)$. Red line is a fit to a Gaussian function, which yields a width at half maximum of $\sim 0.4^\circ$. (b) X-ray rocking curve around the Bragg peak at (200) as a function of the angle Ω. One observes a very broad feature, which can be adjusted to at least two Gaussian distributions (blue lines) of crystallite orientations. (c) Same as in (a) but for a Bragg peak observed along (002) position. Red line is a fit to a Gaussian that yields a full width at half maximum of $\sim 0.3^\circ$. (d) Same as in (b) but for the peak around the (002) position.

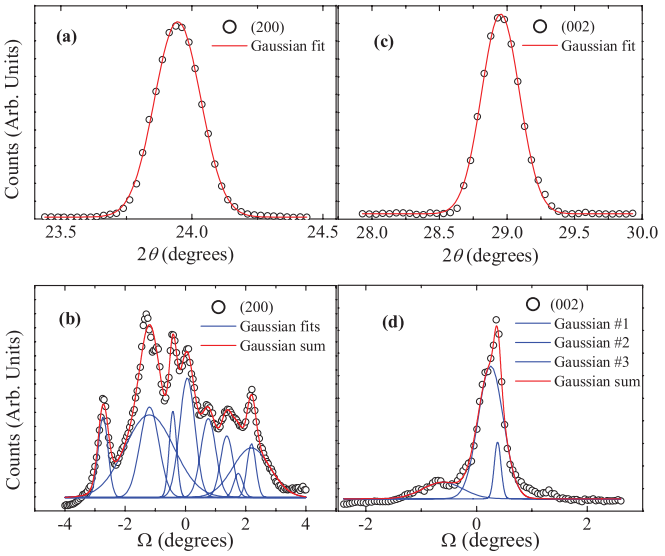

FIG. 6. (Color online) (a) X-ray intensity for a single crystal of $Fe_{1+y}Te_{0.55}Se_{0.45}$ grown by the traveling floating zone method as a function of 2θ for an angular scan around the Bragg peak observed along the (200) position. Red line is a fit to a Gaussian function, which yields a width at half maximum of $\sim 0.2^\circ$. (b) X-ray rocking curve around the Bragg peak at (200) as a function of the angle Ω. One observes a very broad feature, which can be adjusted to a superposition of at least ten Gaussian distributions (blue lines) of crystallite orientations. (b) Same as in (a) but for a Bragg peak observed along (002) position. Red line is a fit to a Gaussian, which yields a full width at half maximum of $\sim 0.3^\circ$. (d) Same as in (b) but for the peak around the (002) position.

observed as the angle 2θ is scanned around the (002) direction. One extracts a FWHM of $\simeq 0.3^\circ$ by fitting its intensity to a Gaussian distribution (red line). Finally, Fig. 5(d) shows the intensity of the Bragg peak observed at the (002) position as a function of the angle Ω. As shown in the figure, to reproduce the observed broad feature one would need to fit it to at least three Gaussian distributions with the widest one having a FWHM of $\gtrsim 2.1^\circ$.

From this detailed comparison between the as-grown and the annealed BRST $Fe_{1+y}Te_{0.6}Se_{0.4}$ single crystals, we can firmly conclude that the annealing process has no, or perhaps just a marginal, effect on the degree of crystallinity of the BRST-grown samples. Although as seen in Fig. 2(a), the behavior of the metallic state, and even the width of the superconducting transition is affected by this treatment and as we shall see below, it also affects $H_{c2}(T)$. In Figs. 6(a) through 6(d), we show a similar rocking curve analysis for a typical TSFZ $Fe_{1+y}Te_{0.55}Se_{0.45}$ single crystal, and as can clearly be seen in Figs. 6(b) and 6(c), the degree of mosaicity in this single crystal is higher (spans over 6°) than what we found for the BRST crystals. Nevertheless, the width of the superconducting transition (see Fig. 1) is considerably sharper than the width of the transition in as-grown BRST crystals [see Fig. 2(a)]. Therefore, from our study, we can state that the mosaicity, or the relative orientation between stacked planes in a single crystal, has virtually no effect on the superconducting properties (such as the width of the transition) of the Fe_{1+y}(Te,Se) series.

Nevertheless, by comparing the EDX data taken on several annealed and nonannealed BRST-grown single crystals, on approximately a dozen of collection sites in each crystal, one notices marked differences between annealed and nonannealed crystals: in average the nonannealed crystals displayed a variability Δy of $\sim 7.7\%$ in the fraction y of interstitial Fe and a $\Delta x \simeq 8.8\%$ in the fraction x of Se, when compared respectively to $\Delta y = 1.8\%$ and $\Delta x = 6.1\%$ for the annealed samples (Δy is the average of the fluctuations in the value of y with respect to its mean value). EDX indicates that the annealing process has virtually no effect on the average value of either x or y, so it just homogenizes both values (specially y) throughout the sample.

However, this observation does not address the origin of, for instance, the "nonmetallic" -like resistivity observed in the TSFZ-grown crystals when compared to the metallic response seen in annealed BRST-grown crystals. For the first ones, we were able to observe clear Bragg peaks and proceed with single-crystal x-ray refinements in shards taken from them, indicating relatively large values for y ranging from 0.07 to 0.12. The crystallographic information file for one of our single crystals is available as Supplemental Material.[32] We also performed EDX analysis on the TSFZ single crystals, finding similar amounts of excess interstitial Fe, and typical values for $\Delta y \simeq 2\%$. Remarkably, for the second ones and despite the physical characterization shown above suggesting relatively high-quality single crystals, we were unable to extract well defined integrated intensities to proceed with single-crystal x-ray refinements. For these crystals, EDX indicates nearly stoichiometric values for y, i.e., $y \sim 0$ although, as previously mentioned, it tends to underestimate the content of Fe

when compared to single-crystal x-ray refinements. These observations indicate that the physical properties of the 11 Fe chalcogenides are nearly oblivious to their degree of mosaicity but depend on the amount of interstitial Fe and on how evenly distributed it is throughout the sample.

IV. SUPERCONDUCTING PHASE DIAGRAM AT HIGH FIELDS

In this section, we compare the high-field superconducting phase diagrams of several crystals synthesized by either the floating zone or the Bridgman-Stockbarger technique. In each case, only the crystals displaying the sharpest superconducting transitions $\Delta T_c = T(0.9\rho_n) - T(0.1\rho_n) \lesssim 1.0$ K (where ρ_n is the value of the resistivity in the normal state just above the superconducting transition) were chosen for the electrical transport measurements under high fields. As indicated by Fig. 2, for the crystals grown by the BRST method, only the annealed samples showed the optimum T_c and the sharpest superconducting transitions among all of the measured samples.

Figures 7(a) and 7(b) show the resistance as a function of temperature for an annealed $Fe_{1+y}Te_{0.6}Se_{0.4}$ single crystal for different fields $\mathbf{H}\|ab$ and $\mathbf{H}\|c$, respectively. Clearly, fields along the c axis produce broader transitions as a function of temperature. Figures 7(c) and 7(d) show the resistance as a function of magnetic fields $\mathbf{H}\|ab$ and $\mathbf{H}\|c$ (up to $H = 45$ T) for the same single crystal and for different temperatures. The transitions become progressively sharper in field as the temperature decreases, consistent with the reduction of vortex fluctuations at lower T. We have also collected similar data sets for several single-crystals grown by the TSFZ method with different Se and Fe contents but the corresponding raw data are not shown here. The stoichiometric fractions of Fe and Se were determined through a detailed single-crystal x-ray diffraction refinement of small shards cleaved off from each single crystal. For these TSFZ samples, the measured superconducting transition temperatures ranged from $T_c \sim 12$ K ($y = 0.26$, x or fraction of Se $= 0.16$) to the optimal T_c value $\gtrsim 14$ K ($y = 0.06$ and $x = 0.44$).

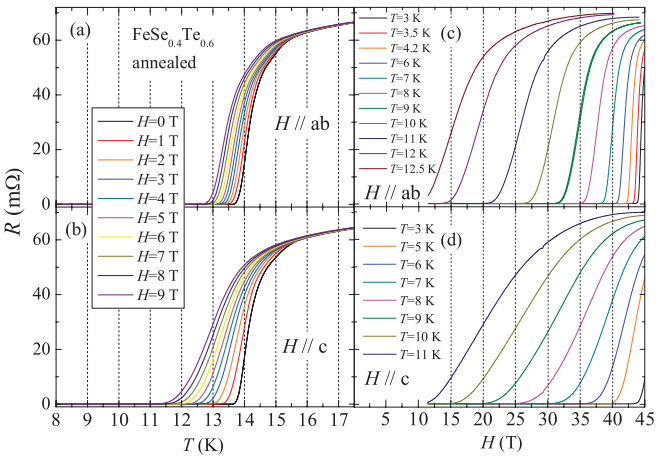

FIG. 7. (Color online) Left panel: resistance as a function of temperature T across the superconducting transition for an annealed $Fe_{1.11}Se_{0.4}Te_{0.6}$ single crystal (nominal stoichiometry) synthesized by the Bridgeman technique, and, respectively, for fields along an in-plane direction (a) and the interplane c axis (b). Right panel: resistance as a function of field H for the same single crystal and for different temperatures, and, respectively, for an in-plane direction (c) and the interplane c axis (d).

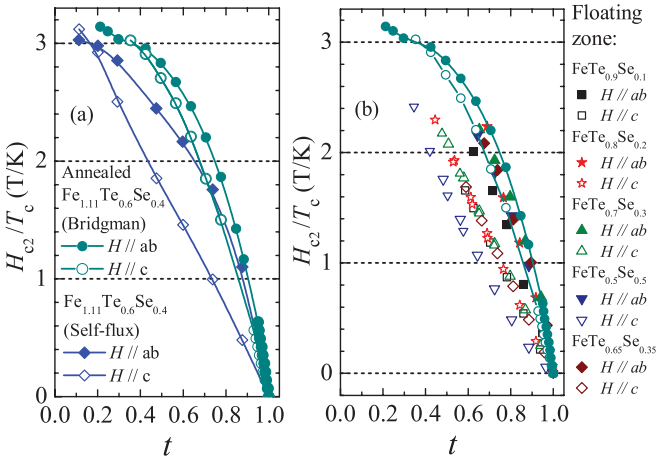

FIG. 8. (Color online) (a) Comparative superconducting phase diagram under high magnetic fields, where the upper critical field H_{c2} is normalized by the superconducting transition temperature T_c, is plotted as a function of the reduced temperature $t = T/T_c$ for two single crystals: for the $Fe_{1+\delta}Se_{0.4}Te_{0.6}$ single crystal in Ref. 20 and for our annealed $Fe_{1.11}Se_{0.4}Te_{0.6}$ (nominal stoichiometry) BRST single crystal, respectively. (b) Superconducting phase diagram for several TSFZ-grown single crystals, where the phase diagram for our annealed $Fe_{1.11}Se_{0.4}Te_{0.6}$ BRST single crystal is also included. Open and solid markers depict the phase boundary between metallic and superconducting states for fields along the c axis and along a planar direction, respectively. All points in both graphs were extracted from the middle point of the resistive transition.

In Fig. 8(a), we compare the superconducting phase diagram at high fields for our annealed BRST $Fe_{1+y}Te_{0.6}Se_{0.4}$ single crystal (circles) with the results of Ref. 20 (squares), and in Fig. 8(b) with the phase diagram obtained for several TSFZ single crystals (various markers excluding circles). Here, all points correspond to the middle point of the resistive transition. In either graph, both the field and the temperature axis are rescaled with the zero-field T_c of each sample (corresponding to the middle point of the zero-field resistive transition).

Here, we use this scaling for comparative purposes only, and not to indicate that these compounds are placed within the dirty limit. The plot in Fig. 7(a) leads to a similar scaling quality when compared with a $H_{c2}(T)/T_c^2$ as a function of T/T_c plot, previously observed in some of the Fe arsenide compounds[35] and which was deemed to be consistent with an effective clean limit scenario due to the small superconducting coherence lengths of the Fe-pnictide compounds. As clearly seen in both figures, the annealed BRST-grown crystal has considerably larger upper critical fields than all the other crystals, particularly for fields along the c axis and at intermediary reduced temperatures, i.e., from ~35–60% larger H_{c2}s for $T/T_c \simeq 0.5$. For $T/T_c \simeq 0.2$, the upper critical field still is ~5% larger than the value reported in Ref. 20. On the other hand, the anisotropy parameter $\gamma \simeq 1.8$ for $T \to T_c$ is slightly smaller than the values reported in Ref. 20 ($\gamma \simeq 2$ for $T \to T_c$), Ref. 24 ($\gamma \simeq 3$ for $T \to T_c$), and Ref. 33 ($\gamma \simeq 3.5$–4

for $T \to T_c$). Given that the level of structural disorder (i.e., mosaicity) seen in crystals showing quite broad transitions and lower T_cs (as-grown BRST crystals) is very similar to the level of mosaicity seen in the annealed crystals, which display relatively sharp transitions, optimum T_c, and higher H_{c2}, one is led to conclude that the superconducting phase diagram of the $Fe_{1+y}Te_{1-x}Se_x$ series for a given value of x is mostly controlled by Δy and Δx, the overall fluctuation on the values of the fraction of interstitial Fe and of the fraction of Se, respectively.

Another intriguing observation is that the superconducting phase diagram for the more Fe stoichiometric samples shows a pronounced downward curvature as T is lowered, which was attributed by several authors to the Pauli-limiting effect,[19,33] in contrast with, for example, the linear dependence seen in Ref. 20 for H_{c2}^c. Indeed, all $H_{c2}/T_c \simeq 3$ ratios shown in Fig. 7 are above the BCS paramagnetic limit, $H_{c2}/T_c = 1.84$, indicating that the Pauli pair breaking is very essential.

A. Two-band analysis of the H_{c2} data

In order to evaluate the contributions of both orbital and Pauli pair-breaking effects for either field orientation and to compare the results with those extracted from heat capacity measurements, we first analyze our $H_{c2}(T)$ data at temperatures close to T_c where the Ginzburg-Landau theory yields[29,33]

$$\left(\frac{H}{H_p}\right)^2 + \frac{H}{H_o} = 1 - \frac{T}{T_c}. \tag{1}$$

Very close to the critical temperature, $(T_c - T)/T_c \ll (H_p/H_o)^2$, the first paramagnetic term in the left-hand side is negligible, and Eq. (1) yields the orbital linear Ginzburg-Landau (GL) temperature dependence, $H_{c2} = H_o(1 - T/T_c)$. At lower temperatures, $(T_c - T)/T_c > (H_p/H_o)^2$, the Pauli-limiting field H_p dominates the shape of $H_{c2}(T) \propto (1 - t)^{1/2}$ even in the GL domain if $H_p < H_o$. The latter inequality is equivalent to the condition that the Maki parameter $\alpha_M \sim H_o/H_p > 1$ is large enough, assuring that the paramagnetic effects are essential. Shown in Fig. 9 is the log-log plot of our $H_{c2}(T)$ as a function of $1 - T/T_c$, where the red lines are fits to Eq. (1). These fits are excellent for the high-field region (excluding the highest fields), but less so very close to T_c, probably due to the relatively large errors in determining temperatures ($\Delta T \sim 25$ mK), which are inherent to transport measurements, or perhaps due to broadening of the resistive transition due to local T_c inhomogeneities. The fit yields $H_p^{\|c} = (72.3 \pm 3.5)$ T and $H_p^{\|ab} = (62.6 \pm 2.4)$ T for the Pauli-limiting field, respectively, for fields along the c axis and along the ab plane, and $H_o^{\|c} = (160.1 \pm 17.3)$ T and $H_o^{\|ab} = (439 \pm 136)$ T for the orbital-limiting fields, which are in very good agreement with those reported in Ref. 33. Defining the effective GL coherence lengths, $\xi_{ab}(T) = \xi_{ab}(1 - T/T_c)^{-1/2}$ and $\xi_c(T) = \xi_c(1 - T/T_c)^{-1/2}$, we obtain a rather small in-plane value of $\xi_{ab} = (\phi_0/2\pi H_o^{\|c})^{1/2} = 14 \pm 4$ Å and an even smaller c-axis value of $\xi_c = \xi_{ab} H_o^{\|c}/H_o^{\|ab} \sim 5.1$ Å, which is shorter than the interplanar distance $c \sim 6$ Å,[34] in agreement with Ref. 33.

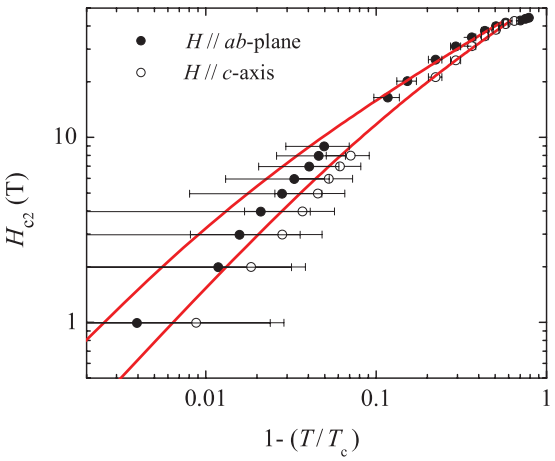

FIG. 9. (Color online) Upper critical fields H_{c2} as functions of $1 - t$, where $t = T/T_c$ is the reduced temperature for an annealed Bridgman-Stockbarger grown single crystal. Red lines are fits to Eq. (1). It yields values for the coherence lengths ξ_{ab} and ξ_c, which are in good agreement with those of Ref. 33.

The phenomenological Eq. (1) only describes the range $T \approx T_c$, but does not take into account the possibility of the FFLO state, which occurs if $\alpha_M > \alpha_c$ is large enough ($\alpha_c \approx 1.8$ for a single parabolic band[25]). To analyze our $H_{c2}(T)$ data at all temperatures and to reveal the microscopic meaning of the scaling fields H_p and H_o, we use a two-band generalization of the Werthamer-Helfand-Hohenberg (WHH) theory[29] in the clean limit, taking into account both orbital and paramagnetic pair breaking, and the possibility of the FFLO with the wave vector $Q(T,H)$. In this case, the equation for H_{c2} is given by

$$a_1 G_1 + a_2 G_2 + G_1 G_2 = 0, \tag{2}$$

$$G_1 = \ln t + 2e^{q^2}\,\mathrm{Re}\sum_{n=0}^{\infty}\int_q^{\infty} du e^{-u^2} \times \left\{\frac{u}{n+1/2} - \frac{t}{\sqrt{b}}\tan^{-1}\left[\frac{u\sqrt{b}}{t(n+1/2)+i\alpha b}\right]\right\}$$

$$G_2 = \ln t + 2e^{sq^2}\,\mathrm{Re}\sum_{n=0}^{\infty}\int_{q\sqrt{s}}^{\infty} du e^{-u^2} \times \left\{\frac{u}{n+1/2} - \frac{t}{\sqrt{b\eta}}\tan^{-1}\left[\frac{u\sqrt{b\eta}}{t(n+1/2)+i\alpha b}\right]\right\}. \tag{3}$$

The FFLO wave vector $Q(T,H)$ is determined self-consistently by the condition that the solution $H_{c2}(T,Q)$ of Eq. (2) is maximum, $a_1 = (\lambda_0 + \lambda_-)/2w$, $a_2 = (\lambda_0 - \lambda_-)/2w$, $\lambda_- = \lambda_{11} - \lambda_{22}$, $\lambda_0 = (\lambda_-^2 + 4\lambda_{12}\lambda_{21})^{1/2}$, $w = \lambda_{11}\lambda_{22} - \lambda_{12}\lambda_{21}$, $t = T/T_c$, and

$$b = \frac{\hbar^2 v_1^2 H}{8\pi\phi_0 k_B^2 T_c^2 g_1^2}, \quad \alpha = \frac{4\mu\phi_0 g_1 k_B T_c}{\hbar^2 v_1^2} = \frac{\pi k_B T_c m}{E_F m_0}, \tag{4}$$

$$q^2 = Q_z^2\phi_0\epsilon_1/2\pi H, \quad \eta = v_2^2/v_1^2, \quad s = \epsilon_2/\epsilon_1. \tag{5}$$

Here, v_l is the in-plane Fermi velocity in band $l = 1,2$, $\epsilon_l = m_l^{ab}/m_l^c$ is the mass anisotropy ratio, μ is the magnetic moment of a quasiparticle, λ_{11} and λ_{22} are the intraband pairing constants, λ_{12} and λ_{21} are the interband pairing con-

stants, and $\alpha \approx 0.56\alpha_M$. The factors $g_1 = 1 + \lambda_{11} + |\lambda_{12}|$ and $g_2 = 1 + \lambda_{22} + |\lambda_{21}|$ describe the strong-coupling Eliashberg corrections. For the sake of simplicity, we consider here the case of $\epsilon_1 = \epsilon_2 = \epsilon$ for which $s = 1$, and H_{ab} is defined by Eqs. (2) and (3) with $g_1 = g_2$ and rescaled $q \to q\epsilon^{-3/4}$, $\alpha \to \alpha\epsilon^{-1/2}$ and $\sqrt{b} \to \epsilon^{1/4}\sqrt{b}$ in G_1 and $\sqrt{\eta b} \to \epsilon^{1/4}\sqrt{\eta b}$ in G_2.[29]

Equation (2), which describes $H_{c2}(T)$ at all temperatures, simplifies close to T_c where it reduces to Eq. (1) with

$$H_o = \frac{48\pi\phi_0 k_B^2 T_c^2}{7\zeta(3)\hbar^2\left[v_1^2 + v_2^2 + \left(v_1^2 - v_2^2\right)\lambda_-/w\right]}, \tag{6}$$

$$H_p = \frac{2\pi k_B T_c}{\mu\sqrt{7\zeta(3)}}, \tag{7}$$

where $\zeta(3) \approx 1.202$. The slope $H'_{c2} = |dH_{c2}/dT|$ is maximum at T_c where Eqs. (2) and (6) yield

$$H'_{c2} = \frac{24\pi\phi_0 k_B^2 T_c}{7\zeta(3)\hbar^2\left(c_+ v_1^2 + c_- v_2^2\right)}. \tag{8}$$

For identical bands, ($v_1 = v_2 = v$, $\lambda_{11} = \lambda_{22}$, $c_+ = c_- = 1/2$), Eq. (8) reduces to the single-band GL expression, $H'_{c2} = \phi_0/2\pi T_c\xi_0^2$, where $\xi_0 = (\hbar v/\pi k_B T_c)[7\zeta(3)/48]^{1/2}$ is the GL coherence length in the clean limit.[29] For the $s^{\pm}$ pairing ($c_+ \to c_- \to 1/2$), the dependence of H'_{c2} on the materials parameters resembles the behavior of $H_{c2}(T)$ in the s^{++} dirty limit; for strong band asymmetry ($\eta \ll 1$ or $\eta \gg 1$), H_{c2} in Eq. (8) is limited by the band with larger Fermi velocity, similar to H_{c2} mostly limited by the band with larger diffusivity for the s^{++} case.[23] Paramagnetic effects decrease the slope of H'_{c2} and reduce the effect of band asymmetry.

Figure 10 shows the fit of the measured $H_{c2}(T)$ to Eq. (2) for $H\|ab$. For this field orientation, the resistive transitions in Fig. 7 (c) are considerably sharper than for $H\|c$. This allowed us to clearly define the middle point of the resistive transition for the traces taken at lower temperatures, increasing the number of the H_{c2} data points. For the sake of simplicity, we consider here the case of $\epsilon_1 = \epsilon_2 = \epsilon$ for which $\gamma = \epsilon^{-1/2}$, and H_{ab} is defined by Eqs. (2) and (3) with rescaled $q \to q\epsilon^{-3/4}$, $\alpha \to \alpha\epsilon^{-1/2}$ and $\sqrt{b} \to \epsilon^{1/4}\sqrt{b}$ in G_1, and $\sqrt{\eta b} \to \epsilon^{1/4}\sqrt{\eta b}$ in G_2.[29] The fit in Fig. 10 was done for $s^{\pm}$ pairing with $\lambda_{11} = \lambda_{22} = 0$, $\lambda_{12}\lambda_{21} = 0.25$, $\eta = 0.9$, $H\|ab$, $\alpha = 2.3$. Equation (2) describes well $H^c_{c2}(T)$, $H^{ab}_{c2}(T)$, and $\gamma_H(T) = b_{\|}(T)/\sqrt{\epsilon}b_{\perp}(T)$, where $b_{\|}(T)$ is the solution of Eq. (2) for $H\|c$.

To see if the observed values of H'_{c2} are at least qualitatively consistent with Eq. (8) and the material parameters of chalcogenides, we use the ARPES data,[43–45] which give $E_F \simeq 20$–50 meV. Taking $E_F = 30$ meV in Eq. (8) yields $H'^{ab}_{c2}(\mathrm{T/K}) \simeq 0.64\gamma(m/m_0)$, so the observed $H'^{ab}_{c2} = H^{ab}_o/T_c = 31.4$ T/K and $\gamma = H^{ab}_o/H^c_o \approx 2.75$ corresponds to the value of $m \simeq 15m_0$ consistent with the ARPES data of $m/m_0 = 3$–20 for different FS pockets.[43] These estimates show that the paramagnetic effects for Fe-11 chalcogenides are indeed essential, and the parameter $\alpha^{ab} = \gamma\alpha$ defined by Eq. (4) is greater than one. For $E_F = 30$ meV and $T_c = 14$ K, we obtain $\alpha^{ab} \simeq 0.13\gamma m/m_0$, giving $\alpha^{ab} \sim 5$. The values of $\alpha > 1$ indicate that paramagnetic pair breaking becomes so strong that it can trigger the FFLO instability at lower temperatures.

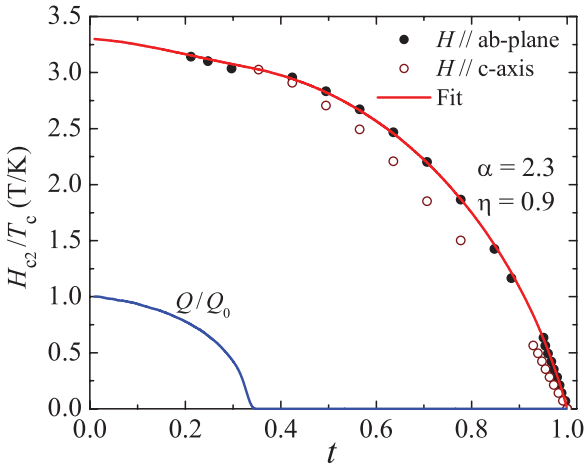

FIG. 10. (Color online) High-field superconducting phase diagram or upper critical field normalized by the superconducting transition temperature at zero field as a function of the reduced temperature, for an annealed BRST-grown $Fe_{1+\delta}Se_{0.4}Te_{0.6}$ single crystal, where the red line is a fit to the model described in the text. Blue line depicts the temperature dependence of the modulation wave vector for a FFLO state, which would explain the shape of the phase boundary at lower temperatures.

As follows from the results shown in Fig. 10, the anisotropy parameter $\gamma_H(T)$ decreases as T decreases. This behavior reflects the significant role of the Zeeman pair breaking in FeSeTe given that $\alpha_{\|} = \alpha/\sqrt{\epsilon} = 2.3$ for $H\perp c$ is well above the single-band FFLO instability threshold, $\alpha \approx 1$.[29] In this case, $\gamma_H(T)$ near T_c is determined by the orbital pair breaking and the mass anisotropy ϵ, but as T decreases, the contribution of the isotropic Zeeman pair breaking increases, resulting in the decrease of $\gamma_H(T)$.

The fit to our experimental data based on the solution of Eq. (2) predicts the FFLO transition for $H||ab$. In this case, Fig. 10 shows that the FFLO wave vector $Q(T)$ appears spontaneously at $T < T_F \approx 0.35T_c \approx 5$ K, corresponding in optimally doped samples to magnetic fields $H \gtrsim 42$ T. Here, $Q(T)$ increases from zero at $T = T_F$ to the maximum Q_0 at $T = 0$, where $Q_0 = 4\pi T_c b(0)^{1/2}/\hbar v_1$. In addition to the strong Pauli pair breaking $\alpha > 1$, the FFLO transition requires weak impurity scattering in the clean limit $\ell \gg \xi$, where ℓ is the mean-free path due to elastic scattering on impurities.[25] The latter condition is likely satisfied in the crystals studied in this work, given the very short coherence lengths $\xi_{ab} \sim 14$ Å and $\xi_c \sim 5$ Å extracted from the fit described above. Thus the chalcogenides are very good candidates to study the FFLO transition by magnetotransport, specific heat, magnetic torque, or NMR measurements.

V. ANALYSIS OF THE CRITICAL REGION

Recent heat-capacity measurements on $FeSe_{0.5}Te_{0.5}$ under field[36] found that it strongly resembles behavior previously observed in the much more anisotropic high-T_c cuprates where strong fluctuation effects have been found to wipe out the phase transition at H_{c2}. In $FeSe_{0.5}Te_{0.5}$, these fluctuations were found to be strongly anisotropic.[36] Here, we proceed to study the critical regime preceding the superconducting transition

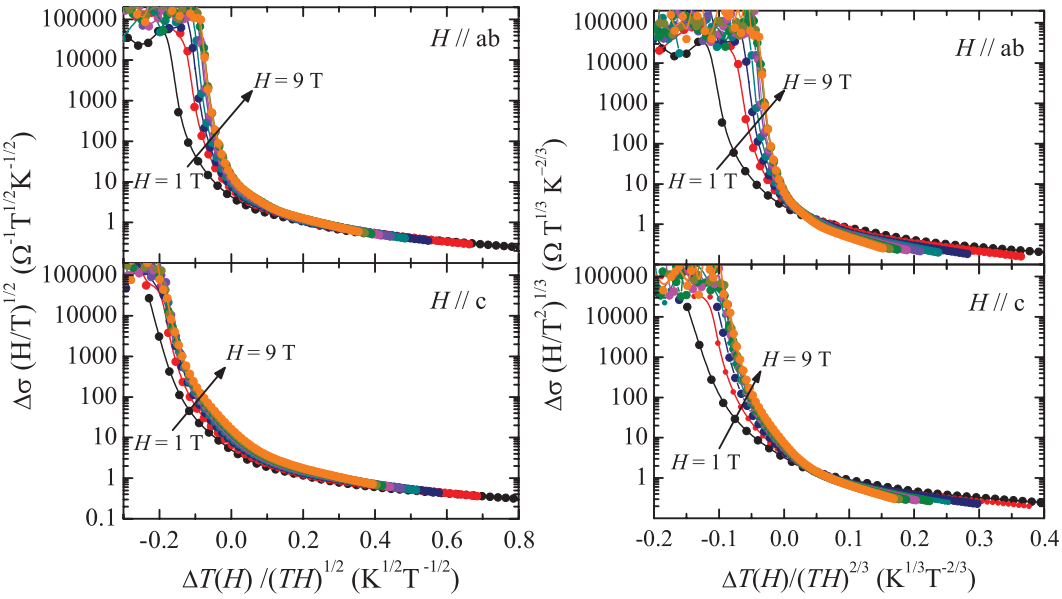

FIG. 11. (Color online) Left panel: $\Delta\sigma(H/T)^{1/2}$ vs $\Delta T(H)/(TH)^{1/2}$ for the annealed BRST single crystal and for both field orientations, as expected for the two-dimensional scaling relation of Eq. (9). Here, $\Delta\sigma = (1/\rho - 1/\rho_n)$, where $1/\rho$ is the resistivity across the superconducting transition and $1/\rho_n$ is the resistivity in the normal state preceding the transition (see main text), while $\Delta T(H) = [T - T_c(H)]$. Right Panel: $\Delta\sigma H^{1/3}/T^{2/3}$ vs $[T - T_c(H)]/(TH)^{2/3}$ as expected for the three-dimensional scaling relation in Eq. (10).

in our annealed BRST-grown single crystals. In the critical region of the metal-to-superconducting transition and in the limit of strong magnetic fields, one expects a scaling form for the thermodynamic functions. At very high fields, if the quasiparticles are confined within the lowest Landau level, the transport of charge carriers becomes nearly one-dimensional along the direction of the applied field. Fluctuation effects close to the superconducting transition are expected to be enhanced by the lower effective dimensionality of the system. In the critical regime, the fluctuation conductivity was calculated in Ref. 37 by including a quartic term in the free energy within the Hartree approximation, and obtained a scaling law for the fluctuation conductivity $\Delta\sigma$ in magnetic fields, in terms of unspecified scaling functions F_{2D} and F_{3D}, valid for two-dimensional and three-dimensional superconductors,[37] respectively:

$$\Delta\sigma(H)_{2D} = \left(\frac{T}{H}\right)^{1/2} F_{2D}\left[\alpha\frac{T - T_c(H)}{\sqrt{TH}}\right], \qquad (9)$$

$$\Delta\sigma(H)_{3D} = \left(\frac{T^2}{H}\right)^{1/3} F_{3D}\left[\beta\frac{T - T_c(H)}{(TH)^{2/3}}\right], \qquad (10)$$

where α and β are characteristic constants of a specific material. Presumably, these functionals remain valid even if the quasiparticles are not confined to just the lowest Landau level, but are placed in a few higher Landau levels, as long as the interaction between quasiparticles in distinct Landau levels remains negligible.[38,39] In the cuprates, either type of scaling has been observed in materials having distinct degrees of electronic/superconducting anisotropies.[40]

We define the contribution of the fluctuations to the conductivity $\Delta\sigma$ as the difference between the normal-state conductivity $\sigma_n = 1/\rho_n$ (ρ_n is the normal-state resistivity) and the measured conductivity $\sigma = 1/\rho$. Here, σ_n is obtained from a polynomial fit of the resistivity in a temperature interval $\Delta T \sim 2T_c$ above T_c, where the contribution of the fluctuations to σ should become negligible. Here, T_c is defined as the middle point of the resistive transition, or the 50%.

In the left panel of Fig. 11, we plot $\Delta\sigma(H/T)^{1/2}$ versus $[T - T_c(H)]/(TH)^{1/2}$ for the annealed BRST single crystal for both field orientations, as expected for the two-dimensional scaling relation in Eq. (9). For fields above a relatively small value of just 4 T and for both orientations, this two-dimensional scaling clearly succeeds in collapsing all the curves over an extended temperature range particularly above T_c. We checked that this statement is still valid if the onset of the resistive transition (90% of the resistance of the normal state) is used as the criteria to define T_c. Given that the high field resistive transitions shown in Fig. 7 are remarkably broad, it is not possible to unambiguously define the functional form of $\rho_n(H)$ in order to also collapse those curves in Fig. 11. To compare this two-dimensional (2D) scaling relation with the three-dimensional one, in the right panel of Fig. 11, we plot $\Delta\sigma H^{1/3}/T^{2/3}$ versus $[T - T_c(H)]/(TH)^{2/3}$ as expected for the three-dimensional case described by Eq. (10). Clearly, the two-dimensional relationship provides a better scaling of the data both above and below T_c. Indeed, in the three-dimensional case, the curves at different fields open like a fan above T_c and also tend to separate from each other below this critical temperature. On the other hand, in the 2D case, the curves above 4 T basically overlap over the entire range. The 2D behavior of fluctuation conductivity, already observed in the Fe arsenides,[41,42] implies that the interplane coherence length ξ_c is smaller or in the order of the interplane spacing as found above, or, equivalently, that the coupling between adjacent superconducting planes is smaller than the intraplane condensation energy. Notice that our scaling analysis is consistent with

the report of very anisotropic superconducting fluctuations according to heat capacity measurements.[36] Two-dimensional scaling also suggests that such fluctuations contribute to the broad transitions seen in Fig. 7, which become considerably sharper at lower temperatures.

VI. DISCUSSION

There are several puzzling aspects in the $Fe_{1+y}Te_{1-x}Se_x$ family that have yet to be understood and/or reconciled. For instance, optical spectroscopy measurements in $Fe_{1.06}Te_{0.88}S_{0.14}$ indicate the absence of a Drude peak in optical conductivity, suggesting the absence of well defined coherent quasiparticles in this material.[46] Although, for $FeSe_{0.42}Te_{0.58}$, the in-plane optical conductivity is found to be indeed describable within a Drude-Lorentz model[47] but with an incoherent response along the interplanar direction.[48] Therefore one could even ask if the concept of Fermi surface would be applicable to these compounds. In sharp contrast, a recent angle resolved photoemission study on $FeSe_{0.42}Te_{0.58}$[45] reveals a Fermi surface which is in relative good qualitative agreement with the generic Fermi surface proposed for the family of Fe pnictides: two concentric hole-like cylindrical surfaces at the Γ point and two electron-like cylinders at the M point of the Brillouin zone, which are characterized by a large, FS-sheet dependent, effective-mass enhancement. This indicates that correlations are particularly relevant for these materials, which is consistent with the size of the anomaly observed in the heat capacity at the superconducting transition[49] or the large H_{c2} reported here and by other groups.[20,24,33] This geometry would be consistent with the observation of a resonance mode characterized by a wave vector connecting both types of cylindrical Fermi surfaces[12] pointing toward an itinerant, nestinglike mechanism for the origin of the spin-fluctuations in these systems. Although, this scenario seems difficult to reconcile with the rather large magnetic moment of 1.6 to 1.8 μ_B for the noninterstitial Fe(I) ion as extracted from careful magnetic susceptibility measurements in superconducting samples,[50] and does not explain the observation of short-range magnetic order in (superconducting samples) for the same wave vector as the one extracted for the magnetically ordered state of $Fe_{1+y}Te$.[6] The interstitial Fe(II) is presumably characterized by an even larger moment of $\sim$2.5 μ_B[6,50] and from the superconducting perspective it should act as a magnetic impurity.

A recent DFT + dynamical mean field theory (DMFT) study suggests that a combination of Hund's rule and structural degrees of freedom, such as the pnictogen height and the bond angle between Fe and the pnictide element, are the key parameters defining the role of correlations, i.e., the degree of localization and therefore the concomitant size of the magnetic moment of Fe in iron pnictide compounds.[51] For instance, the larger the size of the pnictogen atom or equivalently the larger the distance between Fe and this element, or the greater the deviation with respect to the ideal tetrahedral angle of 109.5°, the larger is the degree of localization in the Fe site. Or equivalently, the stronger the correlations on those Fermi surface sheets having a marked t_{2g} character, which should favor the development of a magnetic instability. It is therefore easy to speculate on the role played by the interstitial Fe(II): it should favor local lattice distortions that are likely to further distort the Fe-pnictogen angle away from 109.5° favoring local magnetism in detriment of superconductivity. The larger the content in Fe(II) the stronger this detrimental effect, while larger fluctuations in y could create randomly distributed nearly magnetic patches having a larger Fe(II) content that could lead to pair-breaking effects. This rather simple scenario would explain why the annealed BRST-grown samples display clearer and sharper superconducting transitions when compared to the nonannealed ones despite a similarly poor crystallinity.

As for the presence of the FFLO state,[25] it is presumably sensitive to impurities being difficult to reconcile with the presence of magnetic Fe(II) atoms. However, our results suggest that our BRST-grown samples (annealed as well as nonannealed) are closer to having a nearly stoichiometric Fe content. Furthermore, the low-T upturn in $H_{c2}^{c}(T)$, indicative of the FFLO instability as observed in this work, was also observed by other groups, see, for example, Ref. 24. The interplay between magnetism and the FFLO state is still poorly understood,[52] so its existence in the $Fe_{1+y}Te_{1-x}Se_x$ will only be clarified by future calorimetric, magnetic torque, or NMR measurements at high fields.

Finally, given that the interplane coherence length ξ_c is in the order of the interplanar distance, it is relatively easy to understand why the mosaic spread associated with relative orientation among Fe[Se,Te] planes has little effect on the superconducting properties of these materials. Although the superconducting anisotropy is small, the size of ξ_c implies that the Cooper pairs are virtually localized within the planes thus remaining almost oblivious to the potential pair-breaking effects imposed by the grain boundaries located between the planes.

VII. CONCLUSION

In conclusion, we find that the Fe[Te,Se] planes are well stacked along the c axis, forming domains with well aligned planes spanning a certain coherence length along the c axis. These domains display a small twist with respect to each other, in the order of a degree or less, defining grain boundaries. Our study strongly indicates that these domain boundaries have little or no effect on the superconducting properties of the $Fe_{1+y}Te_{1-x}Se_x$ series. However, a relatively weak disorder in the distribution of interstitial Fe is found to be detrimental to the superconducting properties of the $Fe_{1+y}Te_{1-x}Se_x$ series, broadening the width of the superconducting transition and suppressing the diamagnetic response. We attribute this to local lattice distortions associated with the interstitial Fe(II), which are likely to locally increase the electronic correlations leading to a higher degree of carrier localization favoring magnetism in detriment of superconductivity. In samples displaying the sharpest superconducting transitions and a very clear diamagnetic signal, we observe a mild upturn in the upper critical field at lower temperatures consistent with the Fulde-Ferrel-Larkin-Ovchinnikov instability. These samples display metallic resistivity suggesting also the formation of coherent quasiparticles at lower temperatures in contrast to previous reports,[46] and implying that a relatively mild excess of randomly distributed

Fe(II) atoms may be enough to suppress the phase coherence. Finally, our estimates of the interplane coherence length $\xi_c \sim 5.1 < 6$ Å, where $c \simeq 6$ Å is the interplanar lattice constant, are consistent with the quasi-two-dimensional superconducting fluctuations in the critical region (also observed by other groups[41,42]).

ACKNOWLEDGMENTS

The NHMFL is supported by NSF through NSF-DMR-0084173 and the State of Florida. L.B. is supported by DOE-BES through award DE-SC0002613. J.W., T.G., and T.S. acknowledge support from FSU.

*balicas@magnet.fsu.edu

[1] F. C. Hsu, J. Y. Luo, K. W. Yeh, T. K. Chen, T. W. Huang, P. M. Wu, Y. C. Lee, Y. L. Huang, Y. Y. Chu, D. C. Yan, and M. K. Wu, Proc. Natl. Acad. Sci. USA **105**, 14262 (2008).

[2] M. H. Fang, H. M. Pham, B. Qian, T. J. Liu, E. K. Vehstedt, Y. Liu, L. Spinu, and Z. Q. Mao, Phys. Rev. B **78**, 224503 (2008).

[3] K. W. Yeh, T. W. Huang, Y. L. Huang, T. K. Chen, F. C. Hsu, P. M. Wu, Y. C. Lee, Y. Y. Chu, C. L. Chen, J. Y. Luo, D. C. Yan, and M. K. Wu, Europhys. Lett. **84**, 37002 (2008).

[4] Y. Mizuguchi, F. Tomioka, S. Tsuda, T. Yamaguchi, and Y. Takano, Appl. Phys. Lett. **93**, 152505 (2008); S. Margadonna, Y. Takabayashi, Y. Ohishi, Y. Mizuguchi, Y. Takano, T. Kagayama, T. Nakagawa, M. Takata, and K. Prassides, Phys. Rev. B **80**, 064506 (2009); G. Garbarino, A. Sow, P. Lejay, A. Sulpice, P. Toulemonde, M. Mezouar, and M. Nunez-Regueiro, Europhys. Lett. **86**, 27001 (2009); S. Medvedev, T. M. McQueen, I. A. Troyan, T. Palasyuk, M. I. Eremets, R. J. Cava, S. Naghavi, F. Casper, V. Ksenofontov, G. Wortmann, and C. Felser, Nat. Mater. **8**, 630 (2010).

[5] D. Fruchart, P. Convert, P. Wolfers, R. Madar, J. P. Senateur, and R. Fruchart, Mater. Res. Bull. **10**, 169 (1975).

[6] W. Bao, Y. Qiu, Q. Huang, M. A. Green, P. Zajdel, M. R. Fitzsimmons, M. Zhernenkov, S. Chang, M. Fang, B. Qian, E. K. Vehstedt, J. Yang, H. M. Pham, L. Spinu, and Z. Q. Mao, Phys. Rev. Lett. **102**, 247001 (2009).

[7] S. L. Li, C. de la Cruz, Q. Huang, Y. Chen, J. W. Lynn, J. P. Hu, Y. L. Huang, F. C. Hsu, K. W. Yeh, M. K. Wu, and P. C. Dai, Phys. Rev. B **79**, 054503 (2009).

[8] C. de la Cruz, Q. Huang, J. W. Lynn, J. Li, W. R. Ii, J. L. Zarestky, H. A. Mook, G. F. Chen, J. L. Luo, N. L. Wang, and P. C. Dai, Nature (London) **453**, 899 (2008).

[9] Q. Huang, Y. Qiu, W. Bao, M. A. Green, J. W. Lynn, Y. C. Gasparovic, T. Wu, G. Wu, and X. H. Chen, Phys. Rev. Lett. **101**, 257003 (2008).

[10] J. Zhao, D. -X. Yao, S. Li, T. Hong, Y. Chen, S. Chang, W. Ratcliff II, J. W. Lynn, H. A. Mook, G. F. Chen, J. L. Luo, N. L. Wang, E. W. Carlson, J. Hu, and P. C. Dai, Phys. Rev. Lett. **101**, 167203 (2008).

[11] A. Subedi, L. J. Zhang, D. J. Singh, and M. H. Du, Phys. Rev. B **78**, 134514 (2008).

[12] Y. M. Qiu, W. Bao, Y. Zhao, C. Broholm, V. Stanev, Z. Tesanovic, Y. C. Gasparovic, S. Chang, J. Hu, B. Qian, M. H. Fang, and Z. Q. Mao, Phys. Rev. Lett. **103**, 067008 (2009).

[13] T. Imai, K. Ahilan, F. L. Ning, T. M. McQueen, and R. J. Cava, Phys. Rev. Lett. **102**, 177005 (2009).

[14] Y. Xia, D. Qian, L. Wray, D. Hsieh, G. F. Chen, J. L. Luo, N. L. Wang, and M. Z. Hasan, Phys. Rev. Lett. **103**, 037002 (2009).

[15] K. Nakayama, T. Sato, P. Richard, T. Kawahara, Y. Sekiba, T. Qian, G. F. Chen, J. L. Luo, N. L. Wang, H. Ding, and T. Takahashi, Phys. Rev. Lett. **105**, 197001 (2010).

[16] B. Zeng, G. Mu, H. Q. Luo, T. Xiang, H. Yang, L. Shan, C. Ren, I. I. Mazin, P. C. Dai, and H. -H. Wen, Nat. Commun. **1**, 112 (2010).

[17] T. M. McQueen, Q. Huang, V. Ksenofontov, C. Felser, Q. Xu, H. Zandbergen, Y. S. Hor, J. Allred, A. J. Williams, D. Qu, J. Checkelsky, N. P. Ong, and R. J. Cava, Phys. Rev. B **79**, 014522 (2009).

[18] T. J. Liu, X. Ke, B. Qian, J. Hu, D. Fobes, E. K. Vehstedt, H. Pham, J. H. Yang, M. H. Fang, L. Spinu, P. Schiffer, Y. Liu, and Z. Q. Mao, Phys. Rev. B **80**, 174509 (2009).

[19] H. Lei, R. Hu, E. S. Choi, J. B. Warren, and C. Petrovic, Phys. Rev. B **81**, 094518 (2010).

[20] M. Fang, J. Yang, F. F. Balakirev, Y. Kohama, J. Singleton, B. Qian, Z. Q. Mao, H. Wang, and H. Q. Yuan, Phys. Rev. B **81**, 020509(R) (2010).

[21] L. Lyard, P. Samuely, P. Szabo, C. Marcenat, T. Klein, K. H. P. Kim, C. U. Jung, H. -S. Lee, B. Kang, S. Choi, S. -I. Lee, L. Paulius, J. Marcus, S. Blanchard, A. G. M. Jansen, U. Welp, G. Karapetrov, and W. K. Kwok, Supercond. Sci. Technol. **16**, 193 (2003).

[22] A. Gurevich, S. Patnaik, V. Braccini, K. H. Kim, C. Mielke, X. Song, L. D. Cooley, S. D. Bu, D. M. Kim, J. H. Choi, L. J. Belenky, J. Giencke, M. K. Lee, W. Tian, X. Q. Pan, A. Siri, E. E. Hellstrom, C. B. Eom, and D. C. Larbalestier, Supercond. Sci. Technol. **17**, 278 (2004).

[23] A. Gurevich, Phys. Rev. B **67**, 184515 (2003); Physica C **456**, 160 (2007).

[24] S. Khim, J. W. Kim, E. S. Choi, Y. Bang, M. Nohara, H. Takagi, and K. H. Kim, Phys. Rev. B **81**, 184511 (2010).

[25] P. Fulde and R. A. Ferrell, Phys. Rev. **135**, A550 (1964); A. I. Larkin and Yu. N. Ovchinnikov, Sov. Phys. JETP **20**, 762 (1965); Y. Matsuda and H. Shimahara, J. Phys. Soc. Jpn. **76**, 051005 (2007).

[26] Y. Liu and C. T. Lin, J. Supercond. Nov. Magn. **24**, 183 (2011).

[27] Y. Mizuguchi and Y. Takano, J. Phys. Soc. Jpn. **79**, 102001 (2010).

[28] B. C. Sales, A. S. Sefat, M. A. McGuire, R. Y. Jin, D. Mandrus, and Y. Mozharivskyj, Phys. Rev. B **79**, 094521 (2009).

[29] A. Gurevich, Phys. Rev. B **82**, 184504 (2010).

[30] The detailed crystallographic information file (CIF) for a typical TSFZ single-crystal x-ray refinement with CSD No. 423463 is available at: [http://www.fiz-karlsruhe.de].

[31] J. Yang, M. Matsui, M. Kawa, H. Ohta, C. Michioka, C. Dong, H. Wang, H. Yuan, M. Fang, and K. Yoshimura, J. Phys. Soc. Jpn. **79**, 074704 (2010).

[32] See Supplemental Material at http://link.aps.org/supplemental/10.1103/PhysRevB.84.174517.

[33] T. Klein, D. Braithwaite, A. Demuer, W. Knafo, G. Lapertot, C. Marcenat, P. Rodière, I. Sheikin, P. Strobel, A. Sulpice, and P. Toulemonde, Phys. Rev. B **82**, 184506 (2010).

[34] M. Tegel, C. Löhnert, and D. Johrendt, Solid State Commun. **150**, 383 (2010).

[35]J. Jaroszynski, S. C. Riggs, F. Hunte, A. Gurevich, D. C. Larbalestier, G. S. Boebinger, F. F. Balakirev, A. Migliori, Z. A. Ren, W. Lu, J. Yang, X. L. Shen, X. L. Dong, Z. X. Zhao, R. Jin, A. S. Sefat, M. A. McGuire, B. C. Sales, D. K. Christen, and D. Mandrus, Phys. Rev. B **78**, 064511 (2008).

[36]A. Serafin, A. I. Coldea, A. Y. Ganin, M. J. Rosseinsky, K. Prassides, D. Vignolles, and A. Carrington, Phys. Rev. B **82**, 104514 (2010).

[37]S. Ullah and A. T. Dorsey, Phys. Rev. Lett. **65**, 2066 (1990); Phys. Rev. B **44**, 262 (1991).

[38]Z. Tešanovic and A. V. Andreev, Phys. Rev. B **49**, 4064 (1994).

[39]Z. Tešanovic, L. Xing, L. Bulaevskii, Q. Li, and M. Suenaga, Phys. Rev. Lett. **69**, 3563 (1992).

[40]M. Roulin, A. Junod, and E. Walker, Physica C **260**, 257 (1996); D. H. Kim, K. E. Gray, and M. D. Trochet, Phys. Rev. B **45**, 10801 (1992); U. Welp, S. Fleshler, W. K. Kwok, R. A. Klemm, V. M. Vinokur, J. Downey, B. Veal, and G. W. Crabtree, Phys. Rev. Lett. **67**, 3180 (1991); N. Overend, M. A. Howson, I. D. Lawrie, S. Abell, P. J. Hirst, C. Changkang, S. Chowdhury, J. W. Hodby, S. E. Inderhees, and M. B. Salamon, Phys. Rev. B **54**, 9499 (1996); R. M. Costa, P. Pureur, L. Ghivelder, J. A. Campá, and I. Rasines, *ibid*. **56**, 10836 (1997); S. W. Pierson, T. M. Katona, Z. Tešanovic, and O. T. Valls, *ibid*. **53**, 8638 (1996); R. M. Costa, P. Pureur, M. Gusmão, S. Senoussi, and K. Behnia, *ibid*. **64**, 214513 (2001).

[41]I. Pallecchi, C. Fanciulli, M. Tropeano, A. Palenzona, M. Ferretti, A. Malagoli, A. Martinelli, I. Sheikin, M. Putti, and C. Ferdeghini, Phys. Rev. B **79**, 104515 (2009).

[42]M. Putti, I. Pallecchi, E. Bellinger, M. Tropeano, C. Ferdeghini, A. Palenzona, C. Tarantini, A. Yamamoto, J. Jiang, J. Jaroszysnki, F. Kametani, D. Abraimov, A. Polyanskii, J. D. Weiss, E. E. Hellstrom, A. Gurevich, D. C. Larbalestier, R. Jin, B. C. Sales, A. S. Sefat, M. A. McGuire, D. Mandrus, P. Cheng, Y. Jia, H. H. Wen, S. Lee, and C. B. Eom, Supercond. Sci. Technol. **23**, 034003 (2010).

[43]K. Nakayama, T. Sato, P. Richard, T. Kawahara, Y. Sekiba, T. Qian, G. F. Chen, J. L. Luo, N. L. Wang, H. Ding, and T. Takahashi, Phys. Rev. Lett. **105**, 197001 (2010).

[44]F. Chen, B. Zhou, Y. Zhang, J. Wei, H.W. Ou, J.F. Zhao, C. He, Q.Q. Ge, M. Arita, K. Shimada, H. Namatame, M. Taniguchi, Z.-Y. Lu, J. Hu, and X.-Y. Cui, and D. L. Feng, Phys. Rev. B **81**, 014526 (2010).

[45]A. Tamai, A. Y. Ganin, E. Rozbicki, J. Bacsa, W. Meevasana, P. D. C. King, M. Caffio, R. Schaub, S. Margadonna, K. Prassides, M. J. Rosseinsky, and F. Baumberger, Phys. Rev. Lett. **104**, 097002 (2010).

[46]N. Stojilovic, A. Koncz, L. W. Kohlman, Rongwei Hu, C. Petrovic, and S. V. Dordevic, Phys. Rev. B **81**, 174518 (2010).

[47]C. C. Homes, A. Akrap, J. S. Wen, Z. J. Xu, Z. W. Lin, Q. Li, and G. D. Gu, Phys. Rev. B **81**, 180508 (2010).

[48]S. J. Moon, C. C. Homes, A. Akrap, Z. J. Xu, J. S. Wen, Z. W. Lin, Q. Li, G. D. Gu, and D. N. Basov, Phys. Rev. Lett. **106**, 217001 (2011).

[49]J. Hu, T. J. Liu, B. Qian, A. Rotaru, L. Spinu, and Z. Q. Mao, Phys. Rev. B **83**, 134521 (2011).

[50]J. Yang, M. Matsu, M. Kawa, H. Ohta, C. Michioka, C. Dong, H. Wang, H. Yuan, M. Fang, and K. Yoshimura, J. Phys. Soc. Jpn. **79**, 074704 (2010).

[51]Z. P. Yin, K. Haule, and G. Kotliar, Nature Mater. (2011), doi: 10.1038/nmat3120.

[52]M. Kenzelmann, T. Strassle, C. Niedermayer, M. Sigrist, B. Padmanabhan, M. Zolliker, A. D. Bianchi, R. Movshovich, E. D. Bauer, J. L. Sarrao, and J. D. Thompson, Science **321**, 1652 (2008).